RESEARCH

Design and preparation of Ti–xFe antibacterial titanium alloys based on micro-area potential difference

**Yanchun Xie · Shenshen Cui · Jiali Hu ·
Hailong Yu · Anwu Xuan · Yongcun Wei ·
Yi Lian · Jinhua Wu · Weinan Du · Erlin Zhang**

Abstract Fe was selected as an alloying element for the first time to prepare a new antibacterial titanium alloy based on micro-area potential difference (MAPD) antibacterial mechanism. The microstructure, the corrosion resistance, the mechanical properties, the antibacterial properties and the cell biocompatibility have been investigated in detail by optical microscopy, scanning electron microscopy, electrochemical testing, mechanical property test, plate count method and cell toxicity measurement. It was demonstrated that heat treatment had a significant on the compressive mechanical properties and the antibacterial properties. Ti–xFe (x = 3,5 and 9) alloys after 850 °C/3 h + 550 °C/62 h heat treatment exhibited strong antimicrobial properties with an antibacterial rate of more than 90% due to the MAPD caused by the redistribution of Fe element during the aging process. In addition, the Fe content and the heat treatment process had a significant influence on the mechanical properties of Ti–xFe alloy but had nearly no effect on the corrosion resistance. All Ti–xFe alloys showed non-toxicity to the MC3T3 cell line in comparison with cp-Ti, indicating that the microzone potential difference had no adverse effect on the corrosion resistance, cell proliferation, adhesion, and spreading. Strong antibacterial properties,

Y. Xie · H. Yu (✉) · A. Xuan · Y. Lian
Northern Theater General Hospital, Shenyang 110016, China
e-mail: yuhailong118@aliyun.com

Y. Xie
e-mail: xieyanchungood@163.com

A. Xuan
e-mail: xuanawcyxuan@163.com

Y. Lian
e-mail: lyyl534833577@163.com

S. Cui · J. Hu · E. Zhang (✉)
Key Laboratory for Anisotropy and Texture of Materials, Education Ministry of China, Northeastern University, Shenyang 110819, China
e-mail: zhangel@atm.neu.edu.cn

S. Cui
e-mail: css18846180230@163.com

J. Hu
e-mail: hujiali523@163.com

Y. Wei
Graduate School of Dalian Medical University, Dalian 116051, China
e-mail: weiyongcun1012@163.com

J. Wu · W. Du
Zhejiang Wanfeng Precision Casting Co., Ltd, Shaoxing 312000, China
e-mail: jinhua.wu@wfjyjt.com

W. Du
e-mail: weinan.du@wfjyjt.com

good cell compatibility and good corrosion resistance demonstrated that Ti–xFe alloy might be a candidate titanium alloy for medical applications.

Introduction

Recently, antibacterial metals and alloys, including antibacterial stainless steel, antibacterial titanium alloys and antibacterial cobalt alloys, have obtained much attention worldwide due to their good antibacterial ability, high mechanical properties and non-toxicity, which could reduce clinical infection or inflammation. So far, Cu and Ag elements have been widely selected as antibacterial alloying elements to develop antibacterial alloys (Zhang et al. 2021; Chen et al. 2023; Zhao et al. 2023; Zhang et al. 2022; Cao et al. 2022; Cui et al. 2022). A large number of studies have proved that metal nanoparticles such as copper (Benassai et al. 2021; Jahan et al. 2021; Cui et al. 2022), silver (Benassai et al. 2021; Parambath et al. 2022; Lee et al. 2014), titanium (Seddiki et al. 2014), gold (Parambath et al. 2022; Fanoro et al. 2021), zinc (Seddiki et al. 2014) and their oxides (Zhang et al. 2022; Hu et al. 2020; Pardo et al. 2006; Chen et al. 2016; Dhiman et al. 2021) have strong antibacterial effects and can effectively kill gram-positive bacteria and gram-negative bacteria.

As for the antibacterial mechanism, it can be roughly divided into two hypotheses: metal ion killing mechanism (Slawson et al. 1992; Ning et al. 2015)and contact antibacterial mechanism (Shi et al. 2020; Fu et al. 2022; Fu et al. 2022; Mahmoudi et al. 2022). According to the metal ion killing mechanism, metal elements that have strong antibacterial functions are usually used as alloying elements, such as Cu, Ag and Zn, and metal ion concentration released from metals or alloys must be high enough to obtain high antibacterial ability (Liang et al. 2023; Buyuksungur et al. 2023). For example, it was reported that Cu ion release concentration from titanium alloys must be higher than 0.34 mg/L (Zhang et al. 2013). Although lots of reports have been published on the good cell compatibility and biological function of Cu ions, there are still doubts on the biocompatibility of Cu ions (Moniri Javadhesari et al. 2020; Yang et al. 2021; Zhang et al. 2022). On the other hand, some research indicated that the extract of Cu-containing antibacterial titanium alloys did not exhibit antibacterial ability, suggesting that the Cu ion release concentration did not contribute to the stronger antibacterial property (Shi et al. 2020; Fu et al. 2021; Sim et al. 2022; Liu et al. 2014; Zhang et al. 2016).

More recently, a new antibacterial mechanism has been put forward, a contact antibacterial mechanism based on micro area potential difference (MAPD) (Fu et al. 2022; Wang et al. 2023). According to the MAPD mechanism, there are many micro-scale areas on the material surface, which have different potential due to the inhomogeneous distribution of chemical composition. When bacteria adhere to the surface and are in contact with the surface, the potential difference will promote the ROS expression of the bacteria. When the potential difference is high enough, the ROS expression would be high enough to lead to the death of bacteria. Based on the MAPD mechanism, the metal alloys would have strong antibacterial properties even if the metal ion release concentration is very low or the alloying element ions do not have antibacterial ability. In our previous study, Ti–Au alloy was designed and prepared based on the MAPD mechanism and exhibited as high as > 99.9% antibacterial rate (Fu et al. 2022).

Based on the above consideration and research results, Fe was selected as the alloying element in this paper to develop a new antibacterial titanium alloy and to reveal the effectiveness of MAPD antibacterial mechanism because there is a large difference in the standard electron potential between Ti element and Fe element, which has the potential to produce high MAPD on the surface and thus exhibit strong antibacterial property. In addition, Fe element is much cheaper than Ti, and the addition of Fe would significantly reduce the materials cost. Also, Fe element is a healthy element for human beings, the addition of Fe will not cause metal ion allergy.

Primary results in this work have demonstrated that antibacterial Ti–Fe has been successfully prepared by proper microstructure control based on MAPD for the first time. The alloys showed a slightly better corrosion resistance than cp-Ti and as good cell biocompatibility as cp-Ti. All results suggest that Ti–Fe might be a candidate titanium alloy for biomedical applications.

Experimental

Preparation and characterization of Ti–Fe alloys

Ti–xFe (3, 5 and 9 wt%) ingot was prepared by vacuum arc furnace with commercially pure titanium and high-purity iron as raw materials, and recorded as Ti–xFe-as cast alloys, and solid solution treated at 850 °C for 3 h to dissolve completely Fe element in the matrix, designated as Ti–xFe-T4. Then, Ti–xFe-T4 sample was aged at 550 °C for 62 h and cooled down to room temperature in air, named Ti–xFe-T6. More information on the effect of heat treatment can be found in Fig.s1 and Fig.s2. The experimental samples were briefly noted separately in Table 1. The commercial pure titanium (cp-Ti) was used as a control sample in all experiments. The samples with a dimension of Φ15 mm × 2 mm were sliced from the Ti–xFe ingots or cp-Ti rod for subsequent tests. The chemical constituents of all samples were analyzed by EDS and the results were shown in Table 2.

The microstructure and phase identification were observed under scanning electron microscopy (SEM, Ultra Plus, Zeiss, Germany) and identified by X-ray diffraction (XRD, SmartLab, Rigaku Corporation, Japan) over a 2θ angle of 30–90° at a scanning step of 4°. Kelvin probe force microscopy (KPFM) (SPM-9600, Shimadzu, Japan) was conducted to determine the surface electrode potential distribution. The water contact angle was measured to evaluate the surface wettability on a contact angle instrument (SL200B, Solon, China), and at least three points were measured randomly on each sample, and the mean value was taken as the final data.

Mechanical properties

Microhardness was measured on an MH-500 microhardness meter under a load of 200 g and a holding time of 15 s. At least 10 points were tested to get a

Table 2 EDS analysis results of Ti–Fe alloy (wt%)

Alloys	Elements		
	Ti	Fe	O
cp-Ti	99.86	0.08	0.06
Ti–3Fe	96.94	3.01	0.05
Ti–5Fe	94.91	5.05	0.04
Ti–9Fe	91.03	8.93	0.04

mean value with a standard deviation. A sample with a diameter of 6 mm and a height of 9 mm was used for compressive property testing on AG-XPLUS100KN universal tensile testing machine. Three samples were tested to obtain a mean value with a standard deviation.

Corrosion resistance

Electrochemical properties of the samples were determined by using an three electrodes system on an electrochemical workstation (VersaSTAT V3-400, Princeton Applied Research, USA) at 37 ± 1 °C in 0.9% NaCl solution. The samples served as working electrodes, and saturated calomel electrode (SCE) and platinum electrode served as reference electrode and counter electrode, respectively. According to ISO 10271:2001, the open circuit potential (OCP) curve was recorded for 1 h to determine the open-circuit potential (E_{ocp}). The potentiodynamic polarization curve was acquired at a scanning rate of 1 mV/s from −0.3 V to 0.2 V.

Antibacterial properties

Staphylococcus aureus (*S. aureus*, ATCC 6538) was chosen to evaluate the antibacterial properties. All samples were sterilized with an alcohol lamp. Afterward, the samples were put in a 12-well culture plate and 100 μL bacteria suspension with a concentration

Table 1 Alloy code and corresponding alloy composition and heat treatment rules

Alloy code	Alloy composition	Heat treatment system
Ti–xFe (x = 3, 5, 9)-as cast	Ti–xFe (wt%, x = 3, 5, 9)	As cast
Ti–xFe (x = 3, 5, 9)-T4	Ti–xFe (wt%, x = 3, 5, 9)	As cast+solid solution treated at 850 °C for 3 h
Ti–xFe (x = 3, 5, 9)-T6	Ti–xFe (wt%, x = 3, 5, 9)	Solid solution treated at 850 °C for 3 h+aged at 550 °C for 62 h

of 10^5 CFU/mL was dropped on the surface. Then the samples were incubated for 24 h at 37 °C and relative humidity $\geq 90\%$. After the incubation, the samples with bacteria solution were washed with 0.9% NaCl to remove the bacteria completely from the samples into the washing solution. Afterward, 100 μL of the washing solution was spread on a solid agar plate and cultured for another 24 h, and the antibacterial rate (AR) was calculated by the following formula:

$$AR = \left(CFU_{control} - CFU_{sample}\right)/CFU_{control} \times 100\% \tag{1}$$

where, CFU_{sample} and $CFU_{control}$ are the bacterial colonies number on the test samples and cp-Ti control sample, respectively. Three parallel samples were used for each group.

Cell biocompatibility

Samples were immersed in alpha-modified Minimum Essential Medium (Alpha-MEM, Gibco, USA) supplemented with 10% fetal bovine serum (FBS, Gibco, USA) and 1% Penicillin-Streptomycin (Gibco, USA) under a humidified 5% CO_2 atmosphere at 37 °C for 24 h to prepare extracts for the following cell assessment. MC3T3-E1 cells (cell resource center of Shanghai Institute of Biological Sciences, China) were used as cell lines. During the process, a cell suspension of 2×10^4 cells/cm^2 was incubated in a 96-well plate for 24 h and then the culture was replaced by the extract and cultured for 1, 3 and 5 days. After the incubation, 10 μL Cell Counting Kit-8 (CCK-8, Beyotime, China) assay was piped into each well and incubated for 3 h at 37 °C. Then evaluate the optical density (OD) value by using a microplate reader (Bio-Rad iMARK, USA) at 450 nm.

Cytotoxicity was also assessed by the direct surface contact method. During the process, the samples were placed in a 24-well plate, and a cell suspension of 2×10^4 cells/cm^2 was incubated in it and cultured for 1, 3, and 5 days. After the incubation, 50 μL Cell Counting Kit-8 assay was piped into each well and incubated for 3 h at 37 °C. Then 100 μL of the culture medium was transferred to a 96-well plate to evaluate the optical density (OD) value by using a microplate reader at 450 nm.

The cell relative growth rate (RGR) was calculated according to.

$$RGR = OD_{sample}/OD_{control} \times 100\% \tag{2}$$

where OD_{sample} and $OD_{control}$ are the optical density of the test sample and the control sample, respectively. In this experiment, cp-Ti was used as the control sample.

Statistic

All quantitative tests were repeated three times (n = 3) and the data of average value ± standard deviation were presented. Quantitative statistical analysis of representative results, $p < 0.05$ means statistically significant.

Results

Design of Ti–Fe antibacterial alloys based on MAPD

According to MAPD antibacterial mechanism, the alloy should meet the following requirements to obtain strong antibacterial ability:

(1) There are at least two phases in microstructure;
(2) The two phases have different potentials, and the potential difference between these two phases should be high enough. The higher the potential difference the stronger the antibacterial ability.
(3) One of the two phases should be fine to form many micro-areas with potential differences. Increasing the amount of this micro-area would improve the antibacterial ability.

For titanium alloys, titanium should be alloyed by other elements with different standard electron potential and the difference in the standard electron potential between titanium and the alloying element should be as high as possible. Previous study (Fu et al. 2022) has proven that Ti–Ta alloy with a MAPD of 207 mv and Ti–Au alloy with a MAPD of 272 mv exhibited strong antibacterial ability while Ti–Zr with a MAPD of 74 mv did not have antibacterial ability. As listed in Table 3, the difference in the standard electron potential between Ti and Fe is about (1.19–1.590) v, higher than the value of 0.818v between Ti and Ta alloy system, suggesting that Ti–Fe should also have good antibacterial properties.

Table 3 Electron potential of metal elements

| Elements	Chemical reaction	Standard electron potential, v	Difference in the standard electron potential between Ti element and other elements, v
Ti	$Ti^{2+}+2e=Ti$	− 1.630	0
Zr	$Zr^{4+}+4e=Zr$	− 1.529	0.101
Ta	$Ta^{5+}+5e+=Ta$	− 0.810	0.818
Fe	$Fe^{3+}+3e=Fe$	− 0.037	1.593
	$Fe^{2+}+2e=Fe$	− 0.440	1.19
Au	$Au^{+}+e=Au$	+ 1.692	3.322

In order to form a two-phases microstructure, Ti–Me alloy (Me is the alloying element) should have Ti–Me intermetallic compound at room temperature so that Ti–Me compound could precipitate from matrix during the solidification process or heat treatment. In Ti–Fe binary alloy system, TiFe phase would precipitate from matrix according to the eutectoid reaction so that TiFe phase could be formed during the solidification process or low-temperature ageing treatment.

In Ti–Fe binary phase diagram, as shown in Fig. 1, the eutectoid chemical composition is about 17 wt% (15 at %). When Fe content is higher than 17 wt%, the primary TiFe phase will precipitate from titanium matrix during the casting process, which normally deteriorates mechanical properties, for example, worse plasticity. For example, the Fe content in Ti–Fe alloy should be less than 17 wt% to obtain good comprehensive properties. On the other hand, to obtain TiFe phase, the Fe content should be higher than the solid solubility in α-Ti, 0.44at%, and higher Fe content will result in a high volume fraction of TiFe phase. In addition, research (Niu et al. 2021; Umeda et al. 2021; Sandlöbes et al. 2019) on Ti–Fe binary alloys reported Ti–Fe with 2–6 wt% Fe exhibited good comprehensive mechanical and corrosion properties. Based on consideration, Ti–xFe (x = 3, 5, 9 wt%) alloys were selected in the following studies.

Also, from the Ti–Fe binary phase diagrams, all three alloys have a β-Ti single-phase region beyond

Fig. 1 Phase diagram of Ti–Fe alloy (Massalski et al. 1986)
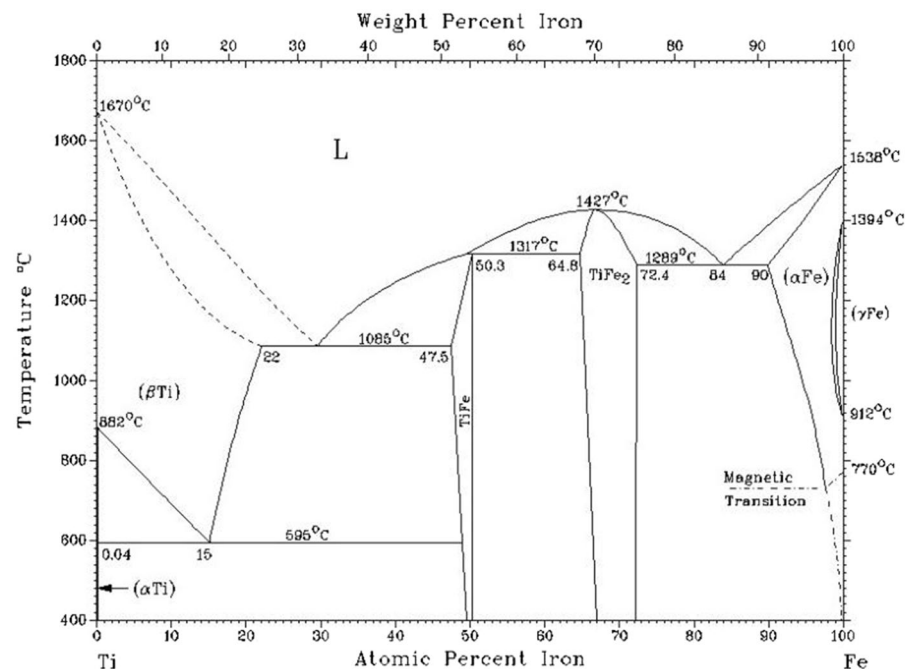
850 °C and the eutectoid reaction temperature is 595 °C, so the aging treatment at 550 °C was selected to precipitate TiFe from the matrix and form nano or micron-sized TiFe phases.

Based on the above considerations, it is possible to prepare a new Ti–Fe antibacterial titanium alloy by ingot metallurgy followed by solid solution and aging treatment. During the process, Ti–xFe with different Fe contents was melted and cast in a non-consumable arc furnace and subjected to solid solution treatment and aging treatment to obtain a fine TiFe phase to get strong antibacterial ability.

Phase identification of Ti–xFe alloys

Figure 2 shows XRD patterns of Ti–xFe alloys at different conditions. It can be seen that Ti–xFe alloys at the as-cast condition mainly consisted of α-Ti and β-Ti, and with the increasing of Fe content, the diffraction intensity of β-Ti became stronger, indicating that more β-Ti phase was formed in the alloy with higher Fe content. After the solid solution treatment at 850 °C for 3 h, Ti–3Fe-T4 alloy mainly consisted of β-Ti and a small amount of α-Ti while Ti–5Fe-T4 and Ti–9Fe-T4 alloys were composed of β-Ti phase only. It can be also found that the diffraction peak position of the β-Ti phase moved toward a high-angle direction in comparison with the standard value, displaying the solid solution of Fe element in the titanium matrix. After the aging treatment, the intensity of the diffraction peaks of α-Ti in Ti–3Fe-T6, Ti–5Fe-T6, and Ti–9Fe-T6 became strong, indicating that more and more α-Ti precipitated from the matrix. However, the diffraction peaks of β-Ti still existed in these alloys even after the long-term aging treatment and more
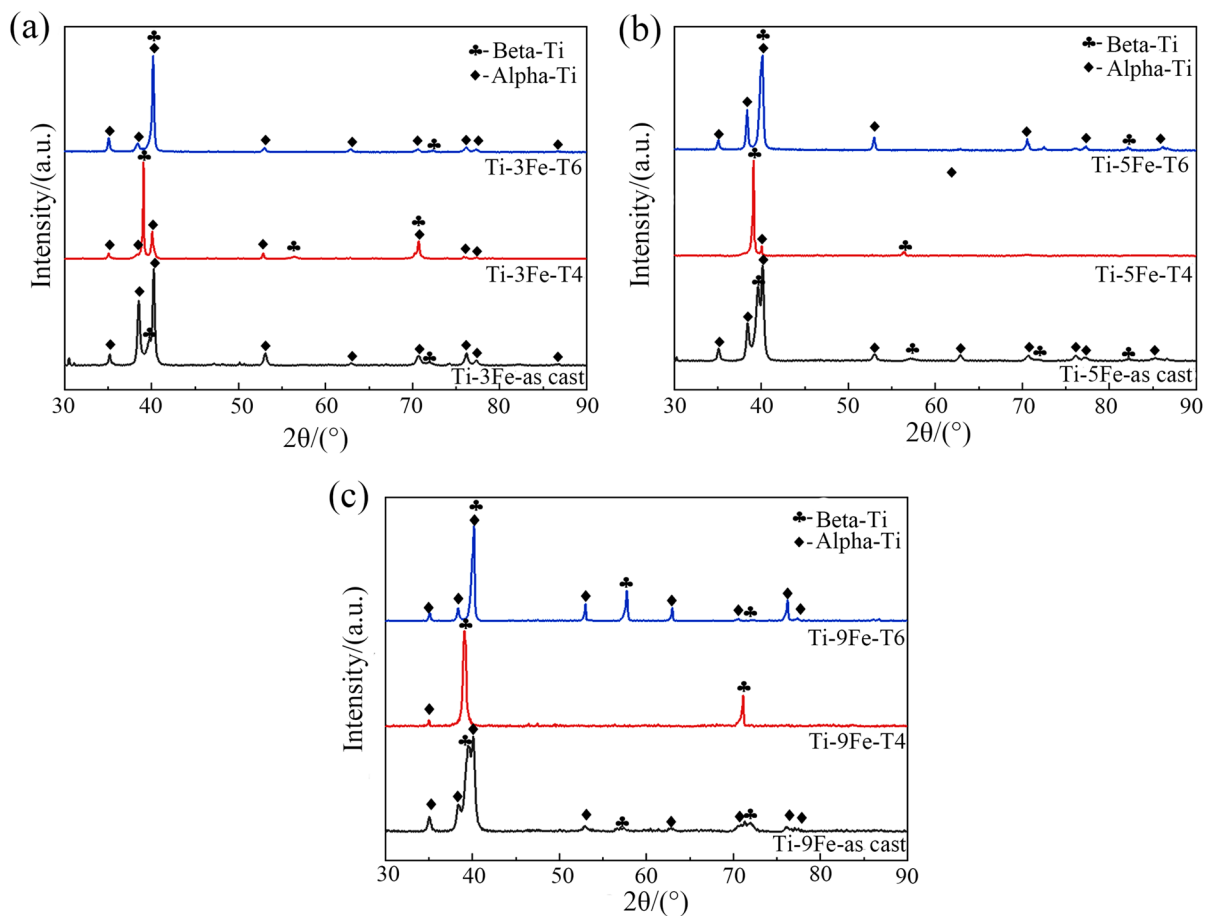

Fig. 2 XRD patterns of Ti–xFe alloys at different conditions a Ti–3Fe; b Ti–5Fe; c Ti–9Fe

β-Ti phase in Ti–xFe with high Fe content. Table 4 shows the phase composition of Ti–xFe alloy.

Microstructure

Figure 3 shows the optical microstructure of Ti–3Fe, Ti–5Fe, and Ti–9Fe alloys at different conditions. At the as-cast condition, Ti–3Fe-as cast and Ti–5Fe-as cast alloys consisted mainly of lathlike α-Ti and β-Ti while Ti–9Fe-as cast alloy mainly consisted of β-Ti and a small amount of α-Ti, indicating that Fe

element has strong β-Ti stabilization ability. After T4 treatment, acicular transformed α-Ti was found in the β-Ti matrix in Ti–3Fe-T4 alloy while very limited transformed α-Ti in Ti–5Fe-T4 and nearly no α-Ti in Ti–9Fe-T4 was observed. After the aging treatment, a coarse basket-net structure was observed in Ti–3Fe-T6 sample while lots of lathlike α-Ti in Ti–5Fe but nearly no α-Ti in Ti–9Fe was found. All these results demonstrate that Fe element had a very strong β-Ti stabilization ability and the aging treatment promoted the β→α phase transformation.

Figure 4 shows the SEM microstructure of Ti–xFe-T6 samples. In the secondary electron image, a large amount of parallel lath-like α-Ti in Ti–3Fe alloy and some lath-like α-Ti in Ti–5Fe alloy but no lath-like α-Ti in Ti–9Fe alloy was observed by SEM. In the high magnification back scanning electron image, the black phase and white phase were found in Ti–3Fe, Ti–5Fe, and Ti–9Fe samples. The EDS results indicate that the Fe element content was different in the

Table 4 Phase constitution of Ti–xFe alloys

Condition	Ti–3Fe	Ti–5Fe	Ti–9Fe
As-cast	α-Ti and β-Ti	α-Ti and β-Ti	β-Ti and α-Ti
T4	β-Ti and acicular α-Ti	β-Ti	β-Ti
T6	α-Ti and β-Ti	α-Ti and β-Ti	β-Ti and α-Ti

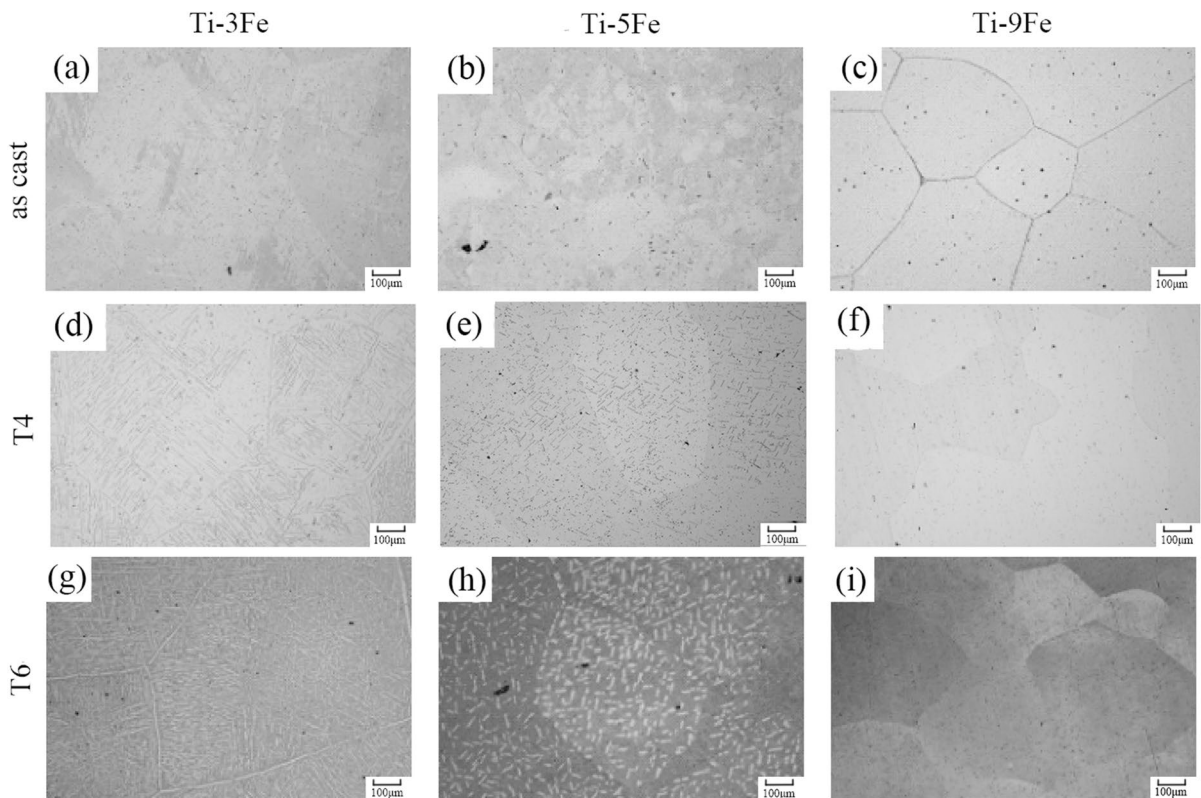**Fig. 3** Optical microstructure of Ti–xFe alloys at different conditions (etched by HF: HNO$_3$: H$_2$O = 1:2:50). **a** Ti–3Fe-as cast, **b** Ti–5Fe-as cast, **c** Ti–9Fe-as cast, **d** Ti–3Fe-T4, **e** Ti–5Fe-T4, **f** Ti–9Fe-T4, **g** Ti–3Fe-T6, **h** Ti–5Fe-T6, **i** Ti–9Fe-T6
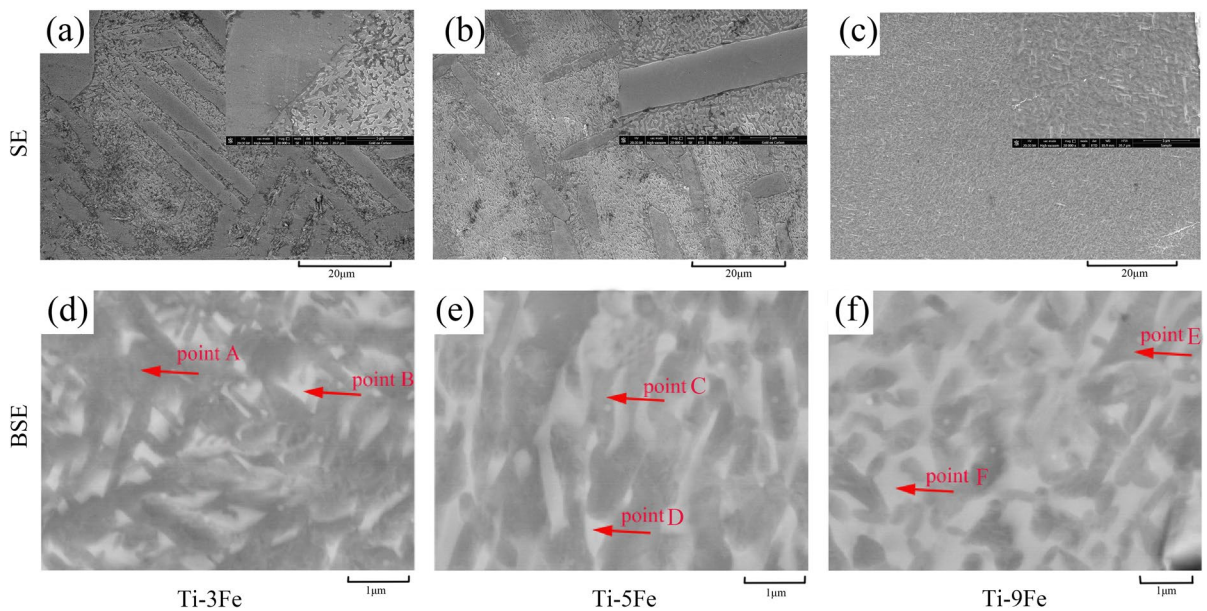
Fig. 4 SEM microstructure of Ti–xFe alloys at T6 condition. Secondary electron image of Ti–3Fe-T6 (**a**), Ti–5Fe-T6 (**b**), Ti–9Fe-T6 (**c**), back scanning electron image of Ti–3Fe-T6 (**d**), Ti–5Fe-T6 (**e**) and Ti–9Fe-T6 (**f**)

Table 5 EDS results at different positions in Fig. 4 in different samples

Materials	EDS position	Elements (wt%)	
		Ti	Fe
Ti–3Fe-T6	Point A	97.60	2.40
	Point B	93.97	6.03
Ti–5Fe-T6	Point C	96.65	3.35
	Point D	91.31	8.69
Ti–9Fe-T6	Point E	94.69	5.31
	Point F	91.41	9.59

black phase and the white phase, while high Fe content in the white phase and low Fe content in the black phase, as listed in Table 5, suggesting that the white phase was the Fe-rich phase and the black phase was the Fe-poor phase. However, no TiFe phase was detected by SEM and EDS in all Ti–xFe-T6 samples.

MAPD

Figure 5 shows the surface morphology and potential distribution determined by SKPFM on the Ti–xFe sample at T4 and T6 conditions. At the T4 condition, only several lathlike α-Ti phases with high potential

were observed on Ti–3Fe and Ti–5Fe samples while nearly no lathlike α-Ti phases with high potential were found on the Ti–9Fe sample. At the T6 condition, besides the lathlike α-Ti phases with high potential in Ti–3Fe-T6 and Ti–5Fe-T6 samples, lots of small areas with high potential were also observed in Ti–3Fe-T6, Ti–5Fe-T6, and Ti–9Fe-T6 samples. The aging treatment process promoted the formation of MAPD in all Ti–xFe samples as expected.

Mechanical properties

Figure 6 shows the change of microhardness of Ti–xFe with the aging time. Meanwhile, the hardness of the as-cast Ti–xFe alloys and the T4-treated Ti–xFe alloys was also shown in the figure at time points of -1 and 0, respectively. For Ti–3Fe alloy, the solid solution treatment increased the microhardness significantly and then the microhardness rapidly decreased during the first 8 h aging process and then decreased slowly with further aging treatment.

Different behavior was observed in the case of Ti–9Fe alloy. The microhardness reached the peak value after 2 h of aging treatment, then decreased fast and gradually with the extension of aging treatment. In all conditions, the hardness increased with the
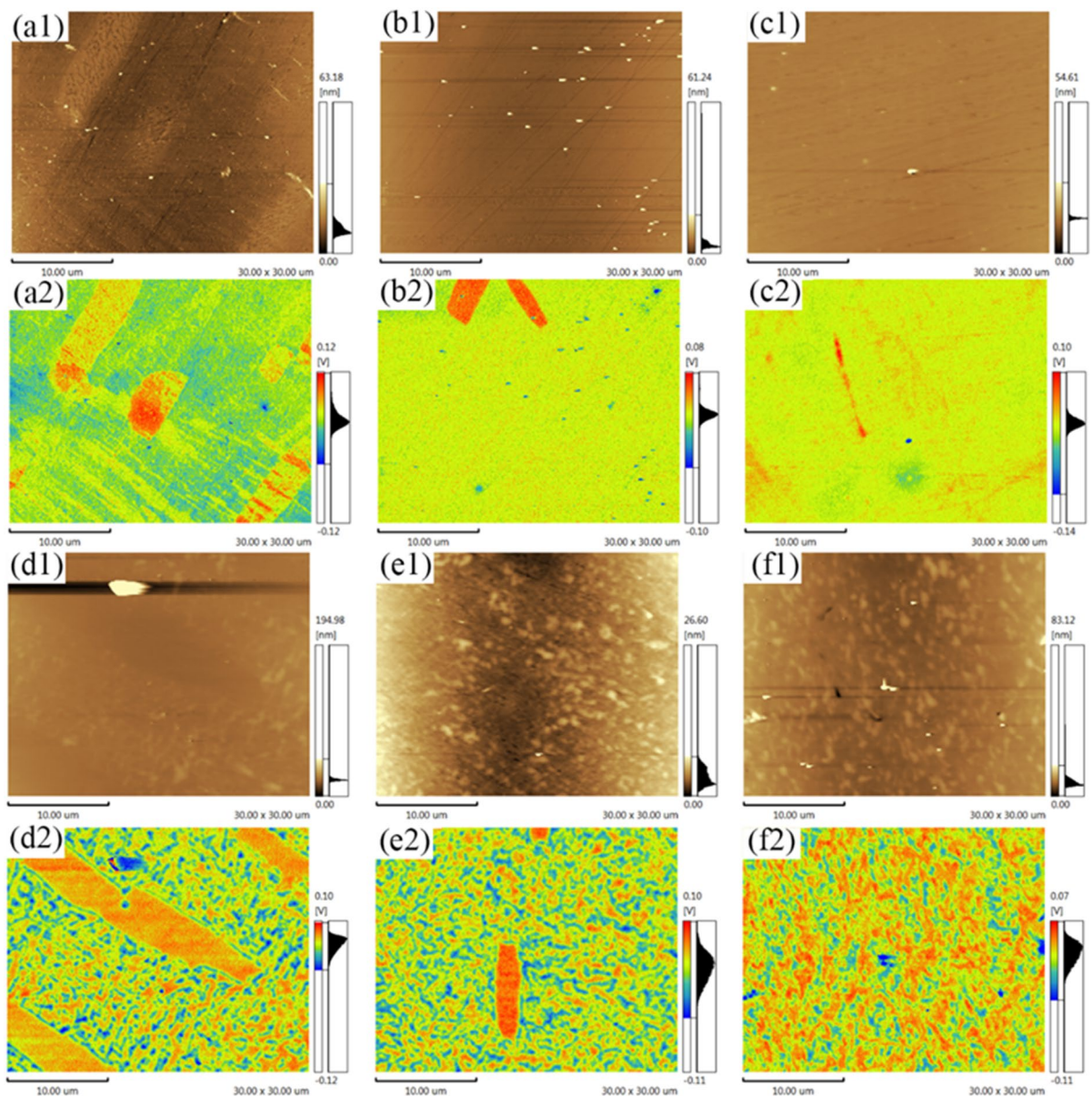
Fig. 5 Surface morphology and potential images on Ti–xFe alloys detected by SKPFM (Scanning area 30 × 30 μm). **a** Ti–3Fe-T4, **b** Ti–5Fe-T4, **c** Ti–9Fe-T4, **d** Ti–3Fe-T6, **e** Ti–5Fe-T6, **f** Ti–9Fe-T6; (1) surface morphology and (2) distribution of potential

addition of the Fe element while Ti–9Fe alloy exhibited 100 HV higher hardness than Ti–3Fe alloy.

Figure 7 shows the typical compressive stress-stain curves of Ti–xFe at different conditions and corresponding strengths and elongation. At the as-cast condition, all Ti–xFe samples showed good compressive strength and plasticity, and both the strength and plasticity increased with the increase of Fe in the Ti–xFe sample, especially the Ti–9Fe-as cast sample exhibited very good plasticity and no broken was observed even after 60% deformation. After T4 treatment, Ti–9Fe-T4 still exhibited as good plasticity and strength as Ti–9Fe-as cast sample, but Ti–3Fe-T4 and Ti–5Fe-T4 samples showed lower plasticity in comparison with the as-cast samples. After 62 h aging treatment, significant improvement in both strength
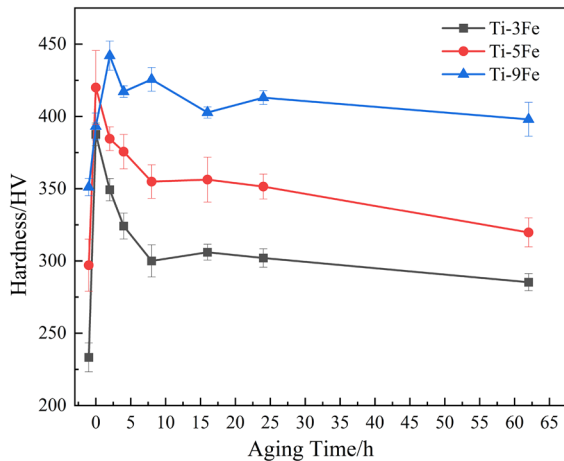
Fig. 6 Microhardness of Ti–xFe sample under different aging time

and elongation was observed in the Ti–3Fe sample while no change in the strength and elongation was found in the case of Ti–5Fe and Ti–9Fe samples.

Corrosion properties

Figure 8a, b show the open circuit potential (OCP) and Tafel curves of Ti–xFe samples at different conditions. The curves of cp-Ti were also shown for comparison. OCP curves of all samples increased with the extension of elapsed time, indicating that a passive film was quickly formed on the surface of all samples. It was noticed that the OCP values at 3600 s of Ti–xFe samples were higher than that of cp-Ti, indicating the addition of Fe element increased the corrosion potential of titanium alloy. In Tafel curves, the addition of Fe element and the following heat treatment moved the curve toward the more noble direction in potential and lower current density directly. Table 6 lists the electrochemical data obtained from the Tafel curve in Fig. 8b using the Tafel extrapolation. The Tafel constants of anode and cathode (β_a and β_c, respectively) were determined by Butler-Volmer equalization, and the polarization resistance (R_p) was calculated according to Stern-Geary equalization (Bakhtiari-Zamani et al. 2022; Cao et al. 2013). The formula for calculating Rp, derived from Tafel extrapolation and Stern-Geary equation, is inversely proportional to the value of i_{corr}, as follows:

$$R_p = \beta_a\beta_c / \left(2.3\left(\beta_a + \beta_c\right)i_{corr}\right) \tag{3}$$
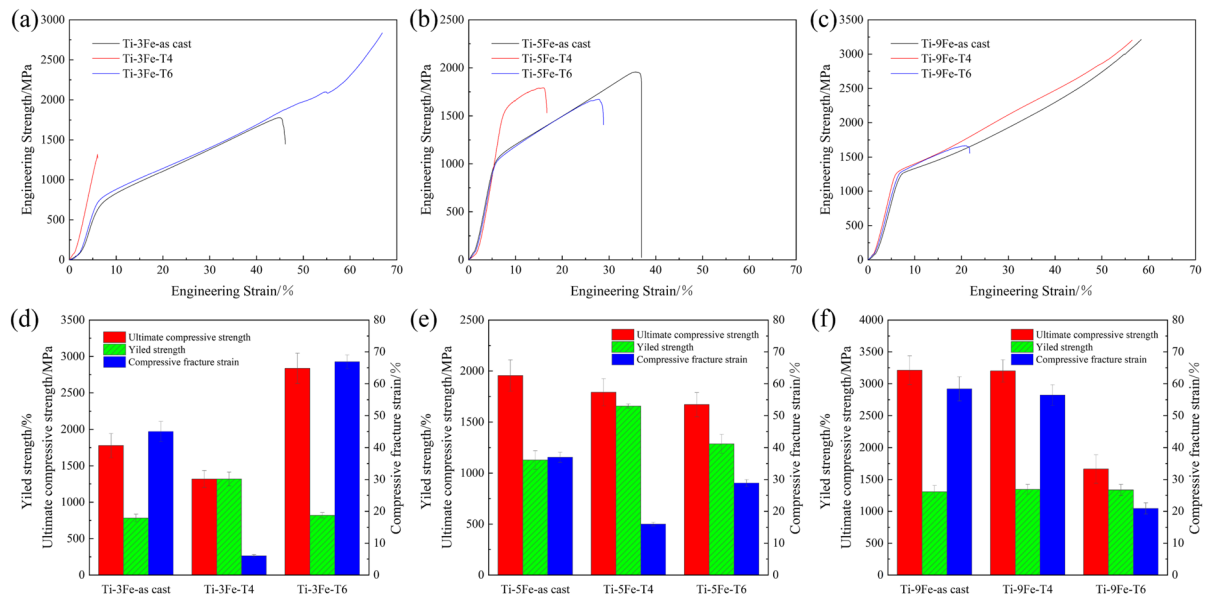

Fig. 7 Typical compressive stress-strain curves of different samples and summaries of strength and elongation. the typical compressive stress curves of Ti–3Fe (**a**), Ti–5Fe (**b**) and Ti– 9Fe (**c**); compressive strength and fracture strain of Ti–3Fe (**d**), Ti–5Fe (**e**) and Ti–9Fe (**f**)
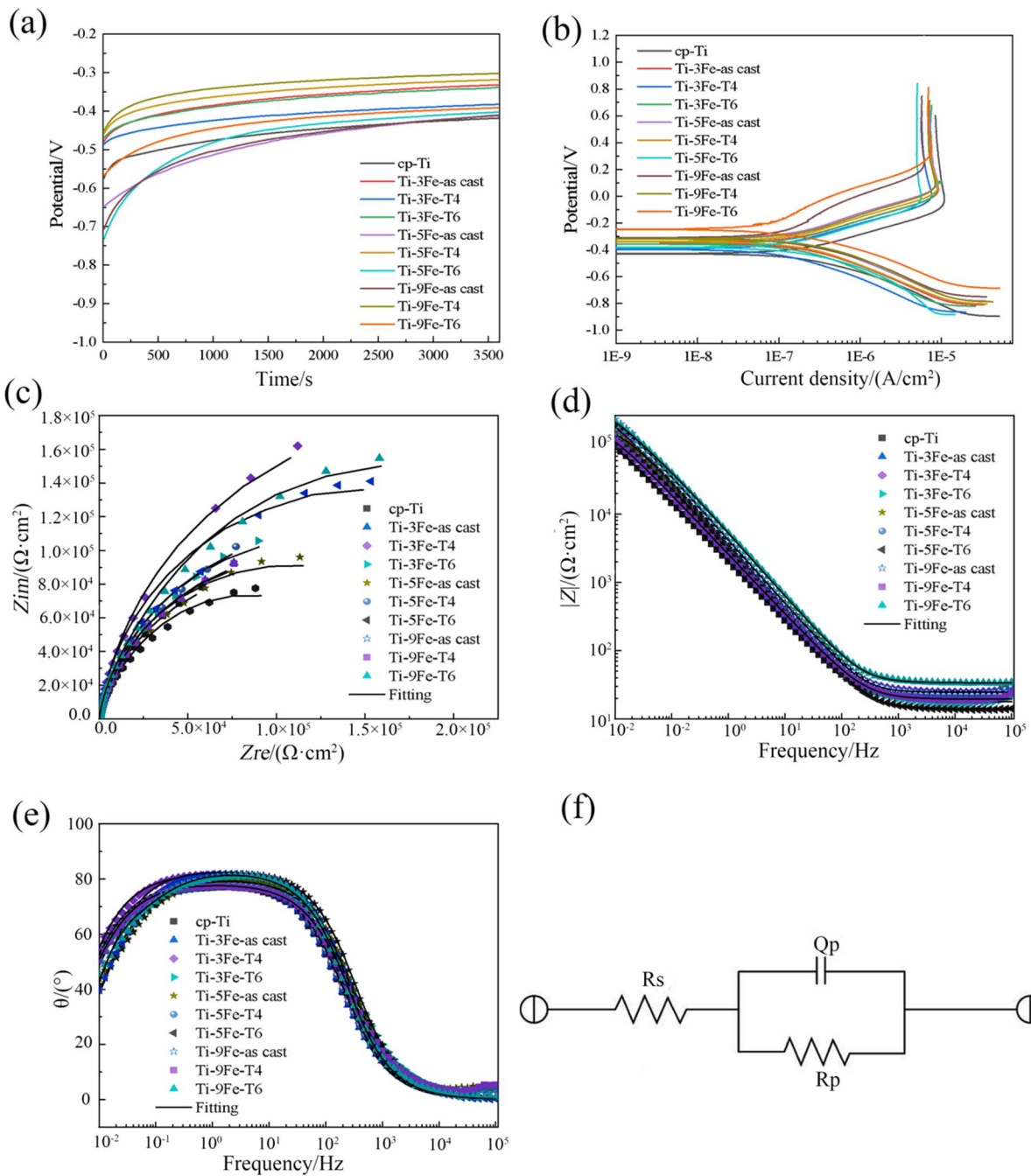
Fig. 8 Electrochemical curves of different samples. **a** open circuit potential curves, **b** Tafel curves, **c** Nyquist, **d** and **e** Bode, **f** equivalent circuit diagram

Figure 8c to e show the EIS curves of Ti–xFe alloys and cp-Ti. All alloys showed nearly similar electrochemical characteristics to cp-Ti. Figure 8f shows the equivalent circuit diagram and Table 7 lists the characteristic values of all samples. In general, Ti–xFe samples showed slightly larger corrosion resistance than cp-Ti, confirming that Ti–xFe alloys exhibited better corrosion resistance than cp-Ti.

Table 6 Electrochemical data of Ti–Fe samples obtained from Tafel curves

Alloys	E_{corr} (mV SCE)	i_{corr} ($\times 10^{-9}$ A/cm)	β_a (mV dec^{-1})	β_c (mV dec^{-1})	Rp (kΩ cm^2)
cp-Ti	− 429.77	306.5	187.4	180.6	130.5
Ti–3Fe-as cast	− 350.54	228.5	184.5	184.3	175.4
Ti–3Fe-T4	− 398.08	148.4	197.3	175.9	272.4
Ti–3Fe− T6	− 358.46	207.2	214.7	184.3	208.1
Ti–5Fe-as cast	− 313.41	188.2	143.5	193.3	190.3
Ti–5Fe-T4	− 338.77	163.7	128.2	178.5	198.2
Ti–5Fe-T6	− 382.9	251.4	167.4	195.1	155.8
Ti–9Fe-as cast	− 312.51	170.3	146.5	141.3	183.6
Ti–9Fe-T4	− 319.07	224.7	143.6	199.2	161.5
Ti–9Fe-T6	− 262.90	164.2	116.8	199.7	195.1

Table 7 Electrochemical data of Ti–Fe samples obtained from EIS curves

Alloys	Rs (Ω cm^2)	Qp (μS cm^{-2} s^{-n})	np	Rp (kΩ cm^2)
cp-Ti	34.31 ± 3.42	170 ± 21.69	0.89 ± 0.04	107.6 ± 78.97
Ti–3Fe-as cast	34.72 ± 3.30	135.43 ± 16.45	0.90 ± 0.04	118.3 ± 72.15
Ti–3Fe-T4	34.91 ± 3.25	95.59 ± 10.87	0.93 ± 0.03	214.7 ± 142.09
Ti–3Fe-T6	36.32 ± 3.73	111.5 ± 14.52	0.90 ± 0.04	136.2 ± 84.64
Ti–5Fe-as cast	34.94 ± 3.36	125.1 ± 15.21	0.89 ± 0.04	133.3 ± 85.32
Ti–5Fe-T4	34.74 ± 3.33	128.5 ± 15.54	0.89 ± 0.03	140.5 ± 95.56
Ti–5Fe-T6	23.46 ± 1.55	62.82 ± 5.16	0.92 ± 0.02	154.3 ± 40.98
Ti–9Fe-as cast	35.55 ± 3.46	75.77 ± 9.11	0.90 ± 0.03	204.6 ± 118.07
Ti–9Fe-T4	34.91 ± 3.51	133.8 ± 17.10	0.89 ± 0.04	121.9 ± 80.88
Ti–9Fe-T6	35.72 ± 3.49	85.93 ± 5.74	0.86 ± 0.03	211.5 ± 194.39

Antibacterial properties

Figure 9 shows the typical bacterial colonies of *S.aureus* after 24 h incubation on different samples. On the cp-Ti sample, there were a large number of bacteria, confirming that cp-Ti does not have antibacterial ability. Lots of bacteria were also observed on Ti–3Fe-T4, Ti–5Fe-T4, and Ti–9Fe-T4 samples, as shown in Fig. 9b, d, indicating that these samples also did not have antibacterial properties. However, there were nearly no bacteria on the T6 treated sample, as shown in Fig. 9e, g, demonstrating that Ti–xFe samples exhibited strong antibacterial ability after T6 treatment. Figure 9 h shows the calculated antibacterial rates. In comparison with cp-Ti, the antibacterial of the T4 treated sample was less than 5% while the T6 samples showed a high antibacterial rate of > 90%.

Figure 10 shows the SEM morphology of *S. aureus* cultured on different samples for 24 h. *S.aureus* clusters with round shapes were found on cp-Ti and Ti–xFe-T4 samples, indicating that the bacteria kept healthy conditions. On the contrary, only several bacteria with broken membranes were found on T6 treated samples, as shown in Fig. 10e to g, suggesting that the samples resisted the bacteria adhesion and the bacteria were in bad condition.

Cell compatibility

Figure 11a, b shows the OD values and relative growth rate of the MC3T3 cell line incubated with the extracts of Ti–xFe samples for 1, 3, and 5 days. With the extension of culture duration, the OD value in all groups increased, indicating that all cells were in a health growth condition. After 1 day of culture, in comparison with the cp-Ti sample, no significant difference was found in the OD among all groups, displaying that no cell toxicity was found among all Ti–xFe samples
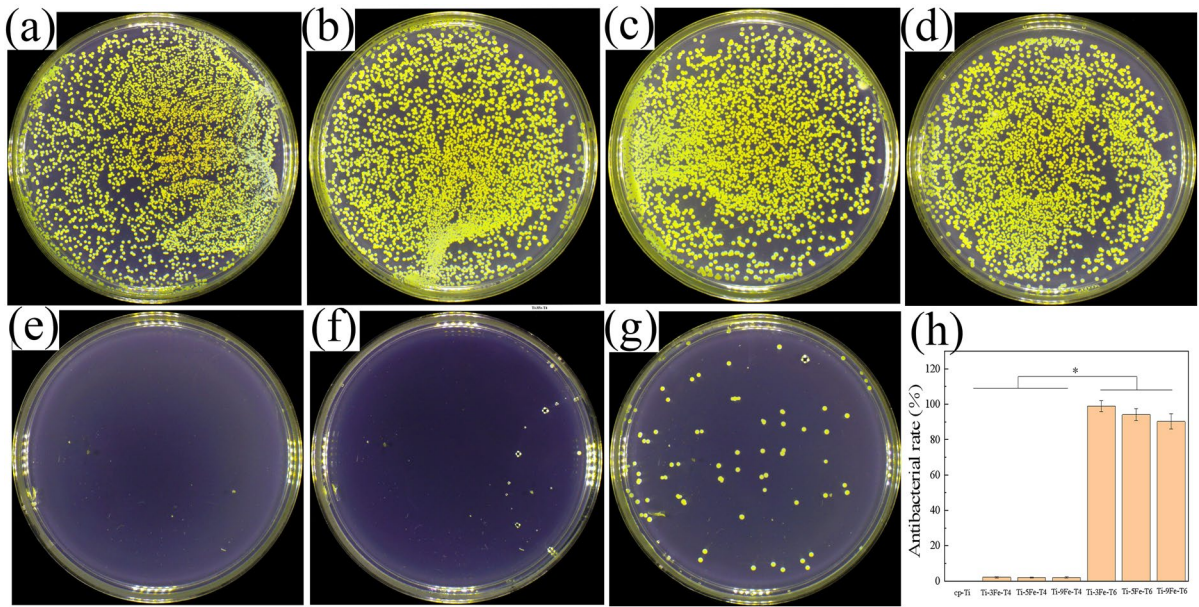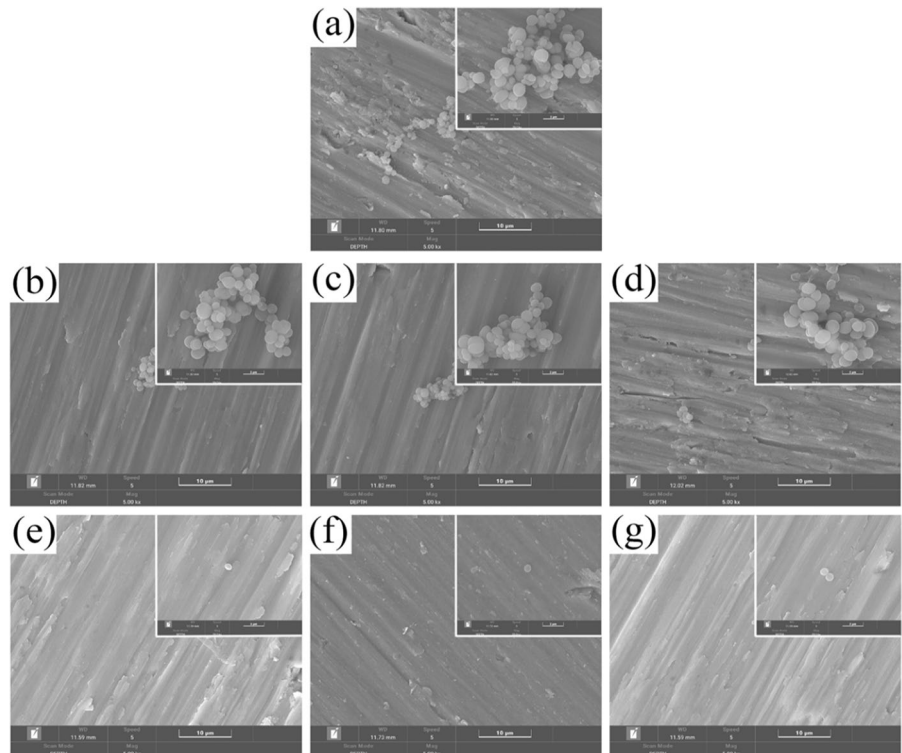
Fig. 9 *S.aureus* colonies co-cultured with different samples for 24 h and corresponding antibacterial rates. **a** cp-Ti, **b** Ti–3Fe-T4, **c** Ti–5Fe-T4, **d** Ti–9Fe-T4, **e** Ti–3Fe-T6, **f** Ti–5Fe-T6, **g** Ti–9Fe-T6, **h** the calculated antibacterial rates

Fig. 10 SEM images of *S.aureus* cultured on different samples for 24 h **a** cp-Ti, **b** Ti–3Fe-T4, **c** Ti–5Fe-T4, **d** Ti–9Fe-T4, **e** Ti–3Fe-T6, **f** Ti–5Fe-T6, **g** Ti–9Fe-T6
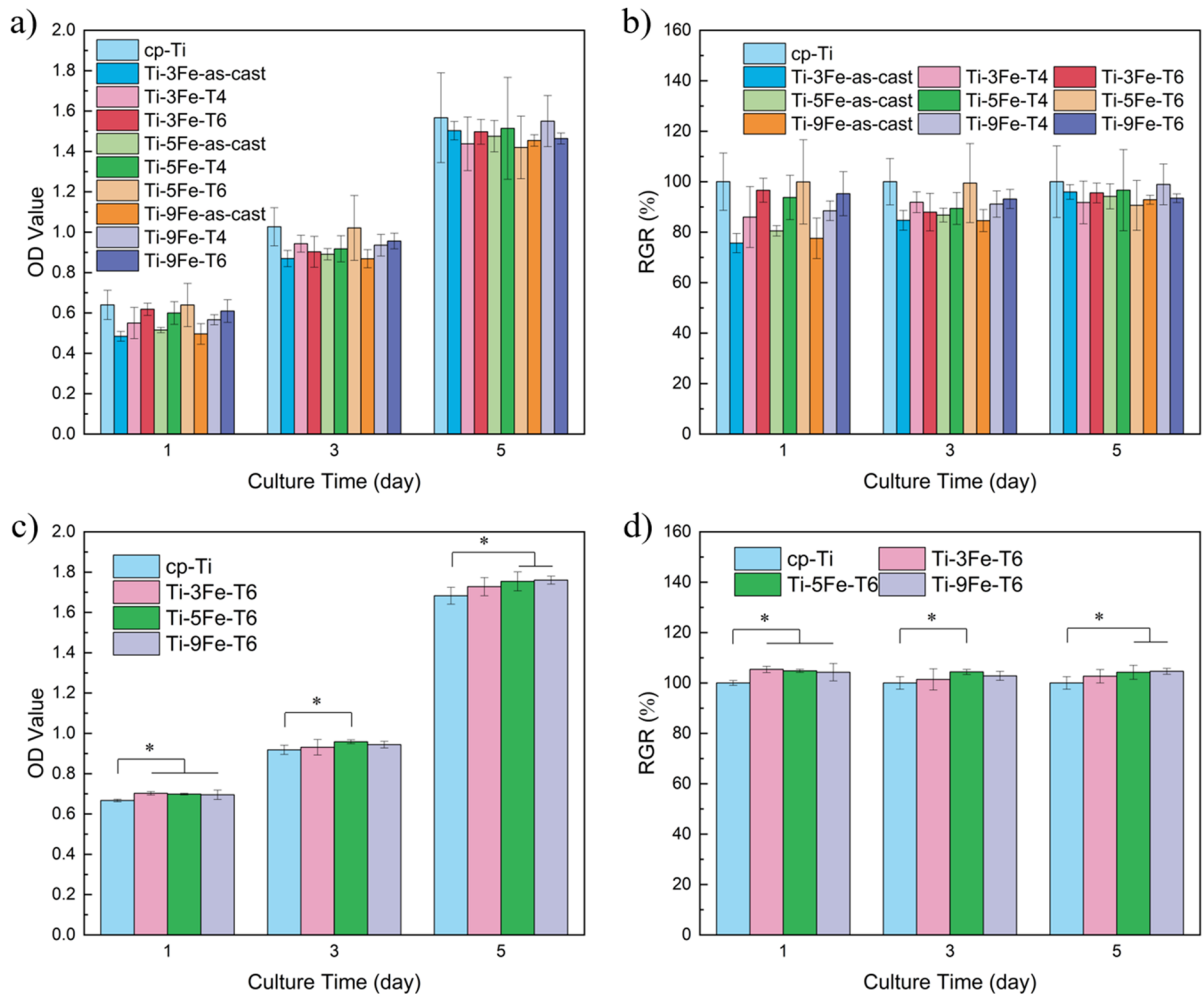
Fig. 11 OD values and relative growth rate of MC3T3 cells incubated in the extracts of Ti–xFe samples for 1, 3, and 5 days. **a** OD value, **b** Relative growth rate ($p > 0.05$) and incu-bated on Ti–xFe-T6 samples for 1, 3, and 5 days. **c** OD value, **d** Relative growth rate (*$p \leq 0.05$)

during the first 24 h incubation. A similar situation was also found in the 3rd day and the 5th day. Figure 11c and d show the OD values and relative growth rate of the MC3T3 cell line incubated on Ti–xFe-T6 samples for 1, 3, and 5 days. With the extension of culture duration, the OD value in all groups increased, indicating that all cells were in a healthy growth condition. After 1 day of culture, the OD values of all groups of Ti–xFe-T6 samples were greater than those of pure titanium samples as compared to cp-Ti samples, no significant difference was found in the OD among Ti–xFe-T6 samples groups, again indicating that no cytotoxicity was detected in all Ti–xFe-T6 samples within 24 h of incubation. A similar situation was found on the third

and fifth day. The difference is only that Ti–5Fe-T6 and Ti–9Fe-T6 show more pronounced differences compared to cp-Ti on the third and fifth day, respectively. In the calculated RGR, as shown in Fig. 11b, d, the RGR of all Ti–xFe alloys was higher than 75%, demonstrating that Ti–xFe samples did not exhibit cell toxicity to MC3T3 cells.

Discussion

Microstructure and MAPD

Ti–Fe alloy is a eutectic alloy system. According to the Ti–Fe phase diagram in Fig. 1, the addition of the

Fe element significantly reduces the β→α transformation temperature to 595 °C, which greatly enlarges the β-Ti phase area. The XRD results in Fig. 2 and the microstructure in Fig. 3demonstrated that the Fe element has a strong β-Ti stabilization ability, which has been proven by other research results (Niu et al. 2021). The solid solution treatment at 850 °C, β-Ti zone, would dissolve Fe element completely to obtain the β-Ti structure by following water quenching. The XRD results and the microstructure confirmed that only the β-Ti phase was found in Ti–5Fe-T4 and Ti–9Fe-T4 samples but α-Ti was also observed in Ti–3Fe-T4 sample, suggesting 3wt% Fe was not enough to resist the β-Ti→α-Ti transformation during the water quenching process. After the aging treatment at 550 °Cfor 62 h, more α-Ti phase precipitated from matrix to form basketnet structure in Ti–3Fe-T6 sample, while some fine α-Ti phase in rod shape precipitated at the grain boundary and inside the grain in Ti–5Fe-T6 sample, as shown in Figs.3h and 4e, and inside grain in Ti–9Fe-T6 sample, as shown in Fig. 4f.

Both XRD patterns and SEM microstructure did not show the precipitation of the TiFe intermetallic phase as expected, strongly demonstrating that the precipitation rate of the TiFe phase was very low. No TiFe phase was also reported in the as-cast Ti–xFe (x = 0.2, 0.5, 1, 2, 3, and 5) alloy (Niu et al. 2021). However, a significant difference in Fe content was found between α-Ti and β-Ti phases, with high Fe content in the β-Ti phase (the white phase) and low Fe content in α-Ti (the black phase), as listed in Table 5. From the Ti–Fe phase diagram in Fig. 1, it can also be found that Fe content in α-Ti is very low, about 0.04 at %. The research results on powder metallurgy Ti-(1–6)wt%Fe also confirmed that the increase in the Fe content was effective in increasing the β-Ti phase volume fraction and refining the α-Ti grain, however, no TiFe phase was reported (Umeda et al. 2021).

Micro-are potential difference (MAPD) is closely related to the chemical composition. The significant difference in Fe content caused by the aging treatment resulted in a significant difference in potential, while the Fe-poor phase exhibited high potential and the Fe-rich phase showed low potential. Although no TiFe phase was found in Ti–xFe alloys, the phase transformation and the redistribution of Fe elements during the aging process promoted the formation of MAPD, as shown in Fig. 5.

Corrosion resistance

cp-Ti already shows very good corrosion resistance in comparison with other bio-metals and alloys, such as stainless steel. OCP results in Fig. 8 indicated that the OCP of Ti–xFe was more positive than cp-Ti during all testing ranges, suggesting that the possessive film formed on the surface of the Ti–xFe alloy could provide more protection against the SBF solution.

Microstructure observation in Fig. 4 and potential distribution in Fig. 5 indicated that there existed a potential difference between Fe-rich β-Ti and Fe-poor α-Ti phases, which should accelerate the electrochemical corrosion between these two phases. However, Tafel curves in Fig. 8 and the calculated electrochemical results in Table 6 demonstrated that Ti–xFe alloys exhibited slightly lower self-corrosion current density and higher corrosion resistance than cp-Ti. Although the polarization resistance of metal Fe is very poor, Fe exists in Ti–Fe alloy as solid solution condition which was confirmed by the microstructure that there are β-Ti or α-Ti phase, rather than TiFe phase or Fe phase. With the consideration of the chemical composition and OCP testing, it was deduced that the addition of Fe accelerated the formation of the passive film on Ti–Fe alloys, which provides good protection against aggressive attack.

Research on as-cast Ti–xFe (x = 0.2, 0.5, 1, 2, 3 and 5) indicated that all Ti–xFe alloys exhibit better corrosion resistance when compared to pure Ti, attributed to a fine grain size formation to induce an increase of growth kinetics on oxide film with higher grain boundary fraction while Ti-2Fe exhibited the best corrosion resistance with the lowest corrosion current density as 0.054 μA/cm^2(Niu et al. 2021).

Mechanical properties

The mechanical property is closely related to the microstructure and the phase constituted in titanium alloy. At the as-cast condition, the mixture of β-Ti and α-Ti phases provided very high compressive yield strength, and with the increasing of Fe content, more β-Ti phase was formed in the alloys which enhanced the plasticity of Ti–Fe alloy, especially Ti–9Fe alloy not break during whole compressive testing. The solid solution results in the formation of acicular α-Ti phases in Ti–3Fe-T4 sample, corresponding to very low plasticity, but complete β-Ti phase in Ti–9Fe-T4

sample, leading to very good plasticity, as shown in Fig. 7c. Further aging treatment promoted the precipitation and growth of lathlike α-Ti in Ti–3Fe-T6 and Ti–5Fe-T6 samples, significantly improving the plasticity in comparison with T4 samples, and the precipitation of transformation α-Ti in Ti–9Fe-T6 sample and significantly reducing the plasticity in comparison with Ti–9Fe-T4 sample.

It has been reported that Ti–3Fe binary alloy could present an ultrahigh strength of 1300 MPa after simple heat treatment (Sandlöbes et al. 2019). Another study indicated the mechanical properties of the as-cast Ti–xFe (x = 0.2, 0.5, 1, 2, 3, and 5) binary alloy increased with the increase of Fe content (Niu et al. 2021). For example, Ti-4Fe alloy presented a yield strength of 558 MPa, ultimate tensile strength of 730 MPa and elongation of 17%.

Van Thyne et al. measured the hardness of Ti–Fe alloy with 0–45 wt% Fe, water quenched from 1000 °C, the hardness peaked at 4% Fe, corresponding to the composition at which β-Ti was retained upon quenching (Thyne et al. 1952). Other research indicated that ω and/or other metastable phases can precipitate upon quenching from the β-Ti phase field in Ti-Mo or Ti–Fe alloy systems such as Ti-4 wt%Fe while ω phase can have a potent strengthening effect (Li et al. 2015). It was also reported that the ω phase forms upon aging at 100 to 500 °C (Vanderpuye 1970; Hickman and OMEGA PHASE PRECIPITATION IN 1969). TiFe intermetallic phase was reported in Ti-20 wt% Fe alloy after 50 h aging at 600 °C. It was reported that the volume fraction increasing of the TiFe phase reduced the hardness of Ti–Fe alloys but the solid solution of Fe element in titanium had a strong strengthening ability. The strengthening induced by Fe is related to the solid solution in titanium matrix β-Ti, but also correlated with the precipitation of ω-phase, which has a very strong strengthening effect. The solid solution of Fe in titanium enhanced the precipitation of ω-phase and improved the hardness by solid solution strengthening and ω-phase strengthing. TiF-phase is softer phase and the formation TiFe phase by the aging treatment reduced the volume fraction of ω-phase, which reduced the hardness. A similar phenomenon was also reported on Ti-20Fe alloy (Jones et al. 2021).

The mechanical properties of Ti–xFe alloy are closely related to the phase constitute, the grains size and the microstructure, in which β-Ti phase strengthening plays a very important role. So, it is possible to change the mechanical properties of Ti–Fe alloy by changing the Fe content or the heat treatment rules.

Antibacterial properties and cell biocompatibility

As stated in the above section, it is believed that the antibacterial activity of titanium alloy is closely related to the surface micro-area potential difference (MAPD). In a previous study, titanium was alloyed by elements with different standard potentials, including Cu and Ag elements by ingot metallurgy and Zr, Ta, and Au by powder metallurgy. In these alloys, intermetallic phases, such as Ti_2Cu, Ti_2Ag, Ti_xZr_y, Ti_xTa_y, and Ti_xAu_y were synthesized in a titanium matrix. These intermetallic phases have a potential difference from titanium matrix, exhibiting different antibacterial abilities. According to the Ti–Fe phase diagram, the TiFe intermetallic phase should be formed during the long-term aging process, but both XRD and SEM did not detect the TiFe phase in Ti–xFe-T6 samples. After T4 treatment, a low amount of β-Ti phase was retained in Ti–9Fe-T4 and a small amount of acicular α-Ti phase precipitated from the matrix in Ti–3Fe-T4 and Ti–5Fe-T4 samples. As a result, the distribution of Fe was relatively homogeneous and the surface MAPD was relatively low, as shown in Fig. 5. Therefore, T4-treated samples did not show any antibacterial ability. After the aging treatment, due to the redistribution of Fe element, high Fe content in β-Ti and low Fe content in α-Ti were found in Ti–xFe-T6 samples, which results in high MAPD on the surface as shown in Fig. 5 and strong antibacterial ability, as shown in Fig. 9.

So far, no report on the antibacterial ability of Fe element or Fe ion has been published. With the results on the antibacterial properties of Ti-Ta, Ti-Mo, and Ti-Au alloys, it is reasonable to believe that the antibacterial ability of titanium alloys or other alloys was closely relative to the surface MAPD and it is possible to design and prepare antibacterial metal alloys based on surface MAPD.

Good cell biocompatibility is always desired for biomedical applications, especially for implant materials. For metal alloys, including titanium alloys, the cell toxicity is mainly from metal ion release, which might cause metal ion allergy. Titanium and titanium

ions have been proven to be biocompatible. Iron is an essential metal for human nutrition, and it is also a vital element for human life (Qin et al. 2021). It plays critical roles in oxygen and electron transport, cell division, differentiation, and regulation of gene expression. According to the Institute of Medicine (IOM), the average daily dietary iron intake is 10 mg to 15 mg in humans (Swanson 2003; Trumbo et al. 2001). The report from the World Health Organization indicated that more than 27% of the world's population experiences iron deficiency anemia (Qin et al. 2021). The cell toxicity test in Fig.11 demonstrated that the extract of Ti–xFe samples did not have cell toxicity, indicating that the Fe ion release from Ti–xFe alloy would not cause any metal ion toxicity. However, more tests are needed to confirm the biocompatibility of Ti–Fe alloy for clinical application. The research results on the toxicity of Ti–xFe to hFOB1.19 also confirmed that all Ti–xFe present a similar cell response and biocompatibility when compared with pure Ti (Niu et al. 2021).

Conclusion

A new antibacterial titanium Ti–Fe alloy was designed and prepared based on the MAPD antibacterial mechanism for the first time. It was demonstrated that heat treatment had a significant on the compressive mechanical properties and the antibacterial properties. The results have shown that Ti–xFe (x = 3,5 and 9) alloys at the solid solution condition did not have antibacterial properties but the alloys at the aging condition exhibited strong antimicrobial properties with an antibacterial rate of more than 90% due to the micro-area potential difference (MAPD) caused by the redistribution of Fe element during the aging process. Ti–xFe exhibited quite different mechanical properties depending on the Fe content and the heat treatment. indifferent Ti phases. High Fe content and the aging treatment improved the strength but reduced the elongation due to the phase constituent. Ti–xFe alloys showed good corrosion resistance and cell biocompatibility compared to pure titanium. The microzone potential difference had no adverse effect on cell proliferation, adhesion, and spreading.

Author contributions YX: methodology, software, validation, investigation, formal analysis, visualization, writing-original draft. SC: software, validation, investigation, formal analysis, visualization, writing. JH: software, validation, investigation, formal analysis, visualization, writing. AX: validation, investigation, formal analysis. YW: validation, investigation, formal analysis. YL: validation, investigation, formal analysis. JW: funding acquisition. WD: funding acquisition. HY: resources, funding acquisition. EZ: conceptualization, resources, writing-review and editing, supervision, funding acquisition.

Declarations

References

Bakhtiari-Zamani H, Saebnoori E, Bakhsheshi-Rad HR, Berto F (2022) Corrosion and wear behavior of TiO_2/TiN duplex coatings on titanium by plasma electrolytic oxidation and gas nitriding. Materials 15(23):8300

Benassai E, Bubba MD, Ancillotti C, Colzi I, Gonnelli C, Calisi N, Salvatici MC, Casalone E, Ristori S (2021) Green and cost-effective synthesis of copper nanoparticles by extracts of non-edible and waste plant materials from vaccinium species: characterization and antimicrobial activity. Mater Sci Eng: C 119:111453

Buyuksungur S, Huri PY, Schmidt J, Pana I, Dinu M, Vitelaru C, Kiss AE, Tamay DG, Hasirci V, Vladescu A, Nesrin H (2023) In vitro cytotoxicity, corrosion and antibacterial efficiencies of Zn doped hydroxyapatite coated Ti based implant materials. Ceram Int 49(8):12570–12584

Cao F, Shi Z, Song G-L, Liu M, Atrens A (2013) Corrosion behaviour in salt spray and in 3.5% NaCl solution saturated with $mg(OH)_2$ of as-cast and solution heat-treated binary Mg–X alloys: X = Mn, Sn, Ca, Zn, Al, Zr, Si, Sr. Corros Sci 76:60–97

Cao S, Zhang ZM, Zhang JQ, Wang RX, Wang XY, Yang L, Chen DF, Qin GW, Zhang EL (2022) Improvement in antibacterial ability and cell cytotoxicity of Ti–Cu alloy by anodic oxidation. Rare Met 41(2):594–609

Chen M, Zhang E, Zhang L (2016) Microstructure, mechanical properties, bio-corrosion properties and antibacterial properties of Ti–Ag sintered alloys. Mater Sci Eng: C 62:350–360

Chen M, Wang X, Hou X, Qiu J, Zhang E, Hu J (2023) Enhanced mechanical, bio-corrosion, and antibacterial properties of Ti–Cu alloy by forming a gradient nanostructured surface layer. Surf Coat Technol 465:129609

Cui SS, Liu S, Nie JJ, Chen DF, Wu XB, Qin GW, Zhang EL (2022) Design and preparation of a biomedical titanium alloy with low elastic modulus and high antibacterial property based on Ti–Mo–Ag system. J Alloys Compd 908:164639

Cui S, Shi A, Xie Y, Yu H, Wei Y, Yang L, Qin G, Zhang E (2022) Feasibility study on Ti-15Mo-7Cu with low elastic modulus and high antibacterial property. Biometals 35(6):1225–1241

Dhiman S, Singh S, Varma A, Goel A (2021) Phytofabricated zinc oxide nanoparticles as a nanofungicide for management of Alternaria blight of Brassica. Biometals 34(6):1275–1293

Fanoro OT, Parani S, Maluleke R, Lebepe TC, Varghese JR, Mavumengwana V, Oluwafemi OS (2021) Facile green, room-temperature synthesis of gold nanoparticles using combretum erythrophyllum leaf extract: antibacterial and cell viability studies against normal and cancerous cells. Antibiotics 10(8):893

Fu S, Zhang Y, Qin G, Zhang E (2021) Antibacterial effect of TiAg alloy motivated by Ag-containing phases. Mater Sci Engineering: C 128:112266

Fu S, Zhang Y, Yang Y, Liu X, Zhang X, Yang L, Xu D, Wang F, Qin G, Zhang E (2022) An antibacterial mechanism of titanium alloy based on micro-area potential difference induced reactive oxygen species. J Mater Sci Technol 119:75–86

Fu S, Zhao X, Yang L, Qin G, Zhang E (2022) A novel Ti-Au alloy with strong antibacterial properties and excellent biocompatibility for biomedical application. Biomater Adv 133:112653

Hickman BS (1969) Omega phase precipitation in, alloys of titanium with transition metals. Trans Met Soc AIME 245:1329–1336

Hu J, Li H, Wang X, Yang L, Chen M, Wang R, Qin G, Chen D-F, Zhang E (2020) Effect of ultrasonic micro-arc oxidation on the antibacterial properties and cell biocompatibility of Ti–Cu alloy for biomedical application. Mater Sci Eng: C 115:110921

Jahan I, Erci F, Isildak I (2021) Facile microwave-mediated green synthesis of non-toxic copper nanoparticles using *Citrus sinensis* aqueous fruit extract and their antibacterial potentials. J Drug Deliv Sci Technol 61:102172

Jones RD, Knowles AJ, Clegg WJ (2021) A binary beta titanium superalloy containing ordered-beta TiFe, alpha and omega. Scripta Mater 200:113905

Lee W, Kim K-J, Lee DG (2014) A novel mechanism for the antibacterial effect of silver nanoparticles on Escherichia coli. Biometals 27(6):1191–1201

Li C-L, Mi X-J, Ye W-J, Hui S-X, Lee D-G, Lee Y-T (2015) Microstructural evolution and age hardening behavior of a new metastable beta Ti–2Al–9.2Mo–2Fe alloy. Mater Sci Engineering: A 645:225–231

Liang S, Jian L, Wang D, Peng F (2023) Enhancement of antibacterial and cytocompatibility of Ti by Zn-doped BST coatings. Mater Lett 338:134018

Liu J, Li F, Liu C, Wang H, Ren B, Yang K, Zhang E (2014) Effect of Cu content on the antibacterial activity of titanium–copper sintered alloys. Mater Sci Eng: C 35:392–400

Mahmoudi P, Akbarpour MR, Lakeh HB, Jing F, Hadidi MR, Akhavan B (2022) Antibacterial Ti–Cu implants: a critical review on mechanisms of action. Mater Today Bio 17:100447

Massalski T, Murray JL, Bennett LH, Baker H (1986) Binary alloy phase diagrams. Ac–Au to Fe–Rh. American Society for Metals, Metals Park

Moniri Javadhesari S, Alipour S, Akbarpour MR (2020) Biocompatibility, osseointegration, antibacterial and mechanical properties of nanocrystalline Ti–Cu alloy as a new orthopedic material. Colloids Surf B 189:110889

Ning CY, Wang XL, Li LH, Zhu Y, Li M, Yu P, Zhou L, Zhou ZN, Chen JQ, Tan GX, Zhang Y, Wang YJ, Mao CB (2015) Concentration ranges of antibacterial cations for showing the highest antibacterial efficacy but the least cytotoxicity against mammalian cells: implications for a new antibacterial mechanism. Chem Res Toxicol 28(9):1815–1822

Niu J, Guo Y, Li K, Liu W, Dan Z, Sun Z, Chang H, Zhou L (2021) Improved mechanical, bio-corrosion properties and in vitro cell responses of Ti–Fe alloys as candidate dental implants. Mater Sci Eng: C 122:111917

Parambath JBM, Ahmady IM, Panicker S, Sin A, Han C, Mohamed AA (2022) Correlation notice on the electrochemical dealloying and antibacterial properties of gold–silver alloy nanoparticles. Biometals 35(6):1307–1323

Pardo A, Merino MC, Carboneras M, Viejo F, Arrabal R, Muñoz J (2006) Influence of Cu and Sn content in the corrosion of AISI 304 and 316 stainless steels in H_2SO_4. Corros Sci 48(5):1075–1092

Qin Z, Su W, Liu P, Ma J, Zhang Y, Jiao T (2021) Facile Preparation of a rhodamine B derivative-based fluorescent probe for visual detection of Iron ions. ACS Omega 6(38):25040–25048

Sandlöbes S, Korte-Kerzel S, Raabe D (2019) On the influence of the heat treatment on microstructure formation and mechanical properties of near-α Ti-Fe alloys. Mater Sci Eng: A 748:301–312

Seddiki O, Harnagea C, Levesque L, Mantovani D, Rosei F (2014) Evidence of antibacterial activity on titanium surfaces through nanotextures. Appl Surf Sci 308:275–284

Shi A, Zhu C, Fu S, Wang R, Qin G, Chen D, Zhang E (2020) What controls the antibacterial activity of Ti–Ag alloy, Ag ion or Ti_2Ag particles? Mater Sci Eng: C 109:110548

Sim JW, Kim JH, Park CH, Hong J-K, Yeom J-T, Lee SW (2022) Effect of phase conditions on tensile and antibacterial properties of Ti–Cu alloys with Ti_2Cu intermetallic compound. J Alloys Compd 926:166823

Slawson RM, Van Dyke MI, Lee H, Trevors JT (1992) Germanium and silver resistance, accumulation, and toxicity in microorganisms. Plasmid 27(1):72–79

Swanson CA (2003) Iron intake and regulation: implications for iron deficiency and iron overload. Alcohol 30(2):99–102

Thyne RJV, Bumps ES, Kessler HD, Hansen M (1952) Phase diagrams of the titanium–aluminum, titanium–chromium-iron, and titanium–oxygen alloy systems. Wright Air Development Center, Roswell

Trumbo P, Yates AA, Schlicker S, Poos M (2001) Dietary reference intakes: vitamin A, vitamin K, arsenic, boron, chromium, copper, iodine, iron, manganese, molybdenum,

nickel, silicon, vanadium, and zinc. J Am Diet Assoc 101(3):294–301

Umeda J, Tanaka T, Teramae T, Kariya S, Fujita J, Nishikawa H, Shibutani Y, Shen J, Kondoh K (2021) Microstructures analysis and quantitative strengthening evaluation of powder metallurgy Ti–Fe binary extruded alloys with (α + β)-dual-phase. Mater Sci Engineering: A 803:140708

Vanderpuye NA, Miodownik AP (1970) The stability of the omega phase in titanium and zirconium alloys. In: Jaffee RI, Promisel NE (eds) The science technology and application of titanium. Elsevier, Pergamon, pp 719–729

Wang C, Hou Y, Fu S, Zhang E, Zhang Z, Bai B (2023) Titanium alloys with varying surface micro-area potential differences have antibacterial abilities and a favorable cellular response. Clin Oral Invest 27(9):4957–4971

Yang J, Qin H, Chai Y, zhang P, Chen Y, Yang K, Qin M, Zhang Y, Xia H, Ren L, Yu B (2021) Molecular mechanisms of osteogenesis and antibacterial activity of Cu-bearing Ti alloy in a bone defect model with Infection in vivo. J Orthop Transl 27:77–89

Zhang E, Li F, Wang H, Liu J, Wang C, Li M, Yang K (2013) A new antibacterial titanium–copper sintered alloy: preparation and antibacterial property. Mater Sci Eng: C 33(7):4280–4287

Zhang EL, Ren J, Li SY, Yang L, Qin GW (2016) Optimization of mechanical properties, biocorrosion properties and antibacterial properties of as-cast Ti–Cu alloys. Biomed Mater 11(6):065001

Zhang E, Zhao X, Hu J, Wang R, Fu S, Qin G (2021) Antibacterial metals and alloys for potential biomedical implants. Bioactive Mater 6(8):2569–2612

Zhang JQ, Cao S, Liu Y, Bao MM, Ren J, Li SY, Zhang EL, Wang JJ (2022) Tribocorrosion behavior of antibacterial Ti–Cu sintered alloys in simulated biological environments. Rare Met 41(6):1921–1932

Zhang Y, Fu S, Yang L, Qin G, Zhang E (2022) A nano-structured TiO$_2$/CuO/Cu$_2$O coating on Ti–Cu alloy with dual function of antibacterial ability and osteogenic activity. J Mater Sci Technol 97:201–212

Zhang S, Yu Y, Wang H, Ren L, Yang K (2022) Study on mechanical behavior of Cu-bearing antibacterial titanium alloy implant. J Mech Behav Biomed Mater 125:104926

Zhao M, Ji X, Li D (2023) Ag + and ca + single implantation and co-implantation induced the cell growth and antibacterial activity of TiN/Ti-6Al-4V. Vacuum 207:111579